Strongly correlated itinerant magnetism near superconductivity in $NiTa_4Se_8$

Nikola Maksimovic,* Ryan Day, Alex Liebman-Peláez, and Fanghui Wan
Department of Physics, University of California, Berkeley, California 94720, USA
and Materials Science Division, Lawrence Berkeley National Laboratory, Berkeley, California 94720, USA

Na-Hyun Jo, Chris Jozwiak, Aaron Bostwick, and Eli Rotenberg
Advanced Light Source, Lawrence Berkeley National Laboratory, Berkeley, California 94720, USA

Sinead Griffin
Materials Science Division, Lawrence Berkeley National Laboratory, Berkeley, California 94720, USA

John Singleton
National High Magnetic Field Laboratory, Los Alamos National Laboratory, Los Alamos, New Mexico 87545, USA

James G. Analytis†
Department of Physics, University of California, Berkeley, California 94720, USA;
Materials Science Division, Lawrence Berkeley National Laboratory, Berkeley, California 94720, USA;
and CIFAR Quantum Materials, CIFAR, Toronto, Ontario M5G 1M1, Canada

(Received 17 August 2022; revised 9 October 2022; accepted 27 October 2022; published 29 December 2022)

Metallic ferromagnets with strongly interacting electrons often exhibit remarkable electronic phases such as ferromagnetic superconductivity, complex spin textures, and nontrivial topology. In this report, we discuss the synthesis of a layered magnetic metal $NiTa_4Se_8$ (or $Ni_{1/4}TaSe_2$) with a Curie temperature of 58 Kelvin. Magnetization data and density functional theory calculations indicate that the nickel atoms host uniaxial ferromagnetic order of about $0.7\mu_B$ per atom, while an even smaller moment is generated in the itinerant tantalum conduction electrons. Strong correlations are evident in flat bands near the Fermi level, a high heat capacity coefficient, and a high Kadowaki-Woods ratio. Density functional theory calculations suggest that electron and hole Fermi surfaces in the ferromagnetic phase are associated with opposite spin polarization. When the system is diluted of magnetic ions, the samples become superconducting below about 2 Kelvin. We discuss possible mechanisms for superconductivity in this family.

DOI: 10.1103/PhysRevB.106.224429

I. INTRODUCTION

The discovery of exotic magnetism and superconductivity in Van der Waals heterostructures has brought into focus the urgency of understanding itinerant magnetism and its implications for nearby superconducting phases. The physics of these materials is thought to be driven by strong correlations arising from their flat-band electronic structure, evoking comparisons with heavy fermion materials whose flat-bands arise from the nearly localized f-electrons of their magnetic ions [1,2]. The observation of comparable phenomena in both graphene heterostructures and heavy fermion metals, including field reentrant superconductivity [3,4], possible triplet superconductivity near itinerant magnetism [5,6], and non-Fermi liquid behavior [7,8] has served to strengthen this connection. Beyond graphene, layered transition-metal dichalcogenides (TMDs) have shown signs of related physics, including the existence of a spin liquid near a Mott insulating phase in 1T′-TaS_2 [2,9], and time-reversal symmetry breaking superconductivity in 4Hb-TaS_2 [10]. Central to the physics of the heavy fermion systems and their exotic superconductivity is the role of correlated itinerant magnetism, but as far as magnetic TMDs are concerned, this physics has not been extensively investigated. The question of whether there are more magnetic TMDs hosting correlated itinerant magnetism potentially near superconducting phases, therefore, remains largely open.

In the itinerant picture of ferromagnetism in metals, an imbalance of occupied spin-up and spin-down states in the conduction bands generate a net magnetic moment [11]. Depending on the exchange splitting and the density of majority and minority spin states, the effective magnetic moment can be much smaller than that originating from localized electrons. As a result of this mechanism, perhaps the clearest observable signature of itinerant ferromagnetism is that the ferromagnetic moment in the ordered phase is considerably

*Corresponding author: nikola_maksimovic@berkeley.edu
†Corresponding author: analytis@berkeley.edu

smaller than that expected of completely localized magnetic dipoles [11–15].

On the other hand, there are fundamental outstanding questions in the study of itinerant ferromagnetism especially in cases where the same electrons that host magnetic modes also interact with each other strongly through the Coulomb force, a situation which calls into question effective single-particle band picture described above. This is thought to be the source of much of the exotic physics in correlated itinerant magnets, driving superconducting pairing in the spin-triplet channel mediated by ferromagnetic spin fluctuations [16], a phenomenon which is historically best exemplified in f-electron magnets [17,18]. In addition, correlated itinerant ferromagnets often exhibit exotic properties [19–21], including strongly renormalized electron effective masses [22,23], topologically nontrivial spin textures [24], and non-Fermi liquid behavior [24–26], all of which could be related to the emergence of ferromagnetically mediated superconductivity [16,27,28]—a leading candidate for realizing topological spin-triplet superconductivity in solids [5].

In this study, we present the growth and characterization of a layered metal $NiTa_4Se_8$ hosting strong electronic correlations and itinerant ferromagnetism. The presence of strongly interacting electrons is evidenced in calorimetry measurements, resistivity measurements, angle-resolved photoemission, and *ab initio* calculations. When the nickel concentration in the samples is reduced, the ferromagnetism apparently disappears and the material superconducts at about 2 Kelvin. We discuss possible mechanisms for the superconductivity given that nickel is a magnetic dopant which orders ferromagnetically at a sufficiently high concentration in this compound. This study serves as a step towards exploring the potential interplay between superconductivity and itinerant ferromagnetism in Ni-intercalated $TaSe_2$, which may be one of many magnetic TMDs that host similar phenomena.

II. CRYSTAL GROWTH

Single crystals were grown by a two-step procedure. First, a precursor was prepared. The elements were combined in a ratio Ni:Ta:Se (x:1.0:2.0), where $x = 0.4, 0.3, 0.08, 0.02$ in four different growth batches. These batches were separately loaded in alumina crucibles and sealed in quartz tubes under a partial pressure (200 torr) of Argon gas. The tube was heated to 670° C—the boiling point of selenium—for 12 hours, and then the temperature was raised to 900° C and kept there for 5 days. The furnace was then shut off and allowed to cool naturally. This reaction yields a free-flowing black powder that was ground with a mortar and pestle separately for each growth batch.

Second, the precursor was loaded with 3-mg/cm^3 iodine in a 21-cm-long quartz tube, evacuated, and placed in a horizontal two-zone furnace. The precursor and iodine were in zone 1 and the other end of the tube (the growth zone) were in zone 2. Both zones were heated to 850° C for 3 hours to encourage nucleation. Then, zone 2 was kept at 850° C while zone 1 was reduced to 700° C. This condition was maintained for 12

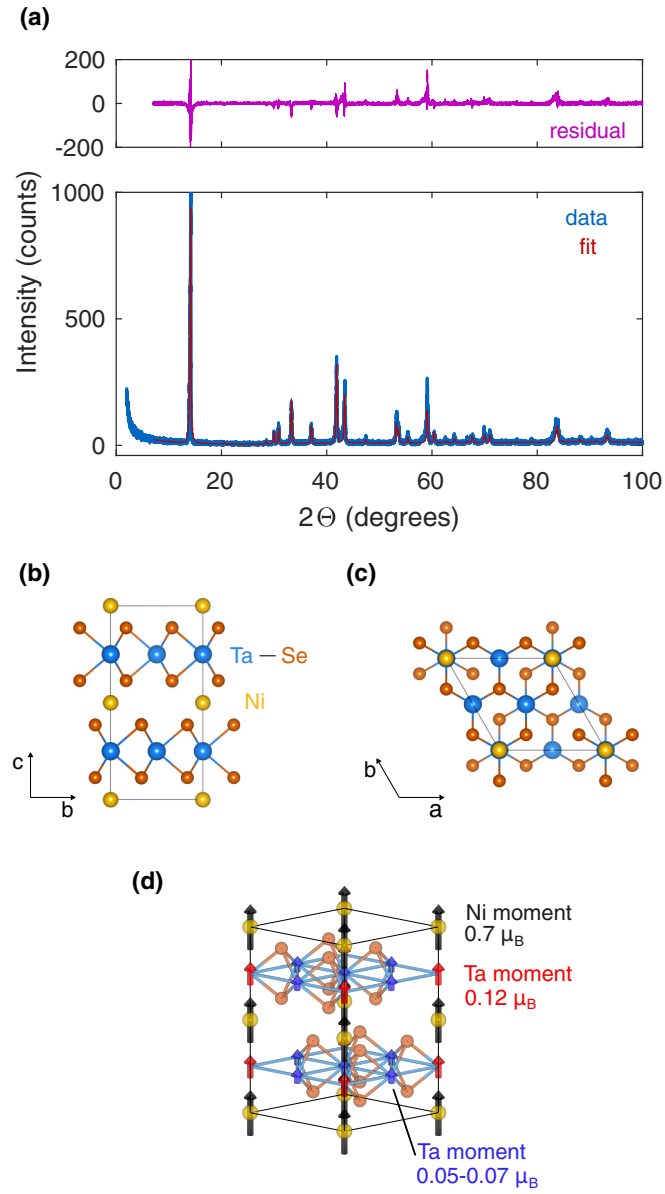

FIG. 1. Experimental crystal structure and calculated magnetic structure of $NiTa_4Se_8$. (a) Powder x-ray diffraction data and refinement (fit shown in red) based on the $P63/mmc$ space group. The residual (the difference between the data and fit) is shown in pink. The lattice parameters extracted from the PXRD refinement are stated in the text. Each prominent peak present in the PXRD data is captured by the refinement based on the crystal structure represented in panels (a) and (b). (b) Crystal structure as viewed along the crystallographic a-axis. The unit cell is outlined by black lines and the crystallographic coordinates are shown in the bottom left. Nickel atoms sit between the $TaSe_2$ layers. (c) Crystal structure viewed along the crystallographic c-axis. The tantalum atoms form a triagonal lattice. The nickel atoms similarly form a triangular lattice with twice the periodicity of that of the tantalum atoms. (d) Visualization of the magnetic structure resulting from magnetic relaxation density functional theory calculations. The spins are given their own color and labeled by the size of the effective moment per atom.

hours to clean the growth zone. Finally, the temperature of zone 1 was raised to 850° C and that of zone 2 was lowered to 700° C. This growth condition was maintained for 5 days after which the furnace was shut off and allowed to cool naturally. Shiny hexagonal crystals up to 5 mm in lateral length were collected from the cold zone. They are easily exfoliated with a scalpel or scotch tape. Crystals of Ta_2NiSe_5, which are easily distinguished from $NiTa_4Se_8$ by both color and morphology were also present in the growth zone.

Energy dispersive x-ray spectroscopy detects an elemental ratio of 0.25:1.00:1.89 (Ni:Ta:Se) for the growth where $x = 0.4$, 0.15:1.00:1.79 for $x = 0.3$, 0.07:1.00:1.86 for $x = 0.08$, and 0.05:1.00:1.80 for $x = 0.02$. suggesting that the samples used in this study are about 5–10% selenium deficient. We believe that this deficiency arises due to the vaporization of selenium during the precursor reaction, which could potentially be adjusted for by adding 5–10% excess selenium to the first stage of the growth procedure. Microdiffraction data indicate that the samples studied are homogeneous (Fig. S10) [29], suggesting that selenium deficiencies are uniformly distributed.

III. RESULTS

The results of powder x-ray diffraction (PXRD) experiments suggest that $NiTa_4Se_8$ ($Ni_{1/4}TaSe_2$) crystallizes in the $P63/mmc$ structure. These experiments are performed on precursor powder resulting from a solid-state reaction from which single crystals were grown using chemical vapor transport as described in the crystal growth section. Every significant peak of the experimental PXRD pattern can be accounted for using the crystal structures schematically shown in Figs. 1(b) and 1(c). Based on these diffraction experiments, we conclude that the material is composed of layered basal planes of $TaSe_2$ in the 2H polymorphic form and there are no significant side phases in the precursor powders. $NiTa_4Se_8$ appears to be isostructural to $Fe_{1/4}TaSe_2$ [30] and $MnTa_4S_8$ [31], other doped transition metal dichalcogenides. Between the sheets of $TaSe_2$, the nickel atoms sit between the tantalum atoms in the neighboring layers. The nickel atoms themselves form a trigonal layer with twice the a-axis periodicity of the tantalum atoms. The crystal structure parameters determined from powder x-ray diffraction refinement are $a = 6.878(6)$ Å and $c = 12.506(5)$ Å.

Figure 1(d) shows the results of magnetic relaxation calculations, the details of which are given in the Supplemental Materials [29]. We find that all the magnetic moments point along the crystallographic c-axis. A moderate magnetic moment of $0.7\mu_B$ per ion lies on the nickel site, while significantly smaller magnetic moments are generated on the tantalum sites—$0.12\mu_B$ per atom in the tantalum atoms lying directly underneath or above the nickel atoms, and 0.05–0.07 μ_B per atom in the rest of the tantalum atoms. These calculations will prove useful in interpreting the results of physical and magnetic properties measurements.

Figure 2 shows the results of low-temperature physical and magnetic properties characterization experiments on single crystal samples. A spontaneous magnetization develops below a Curie temperature of $T_C = 58$ K [Figs. 2(a) and 2(b)], as indicated by the splitting of magnetization curves collected

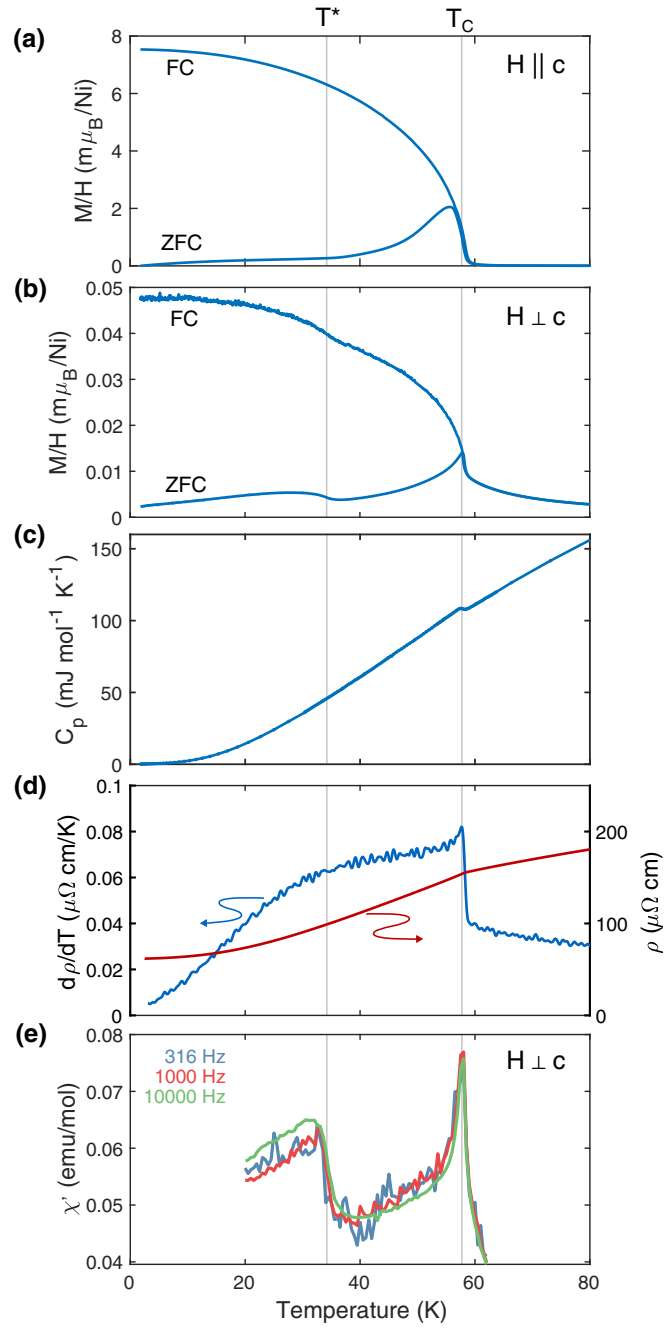

FIG. 2. Physical and magnetic properties of $NiTa_4Se_8$. [(a),(b)] Magnetic susceptibility measured in a field of 100 Oe in the field-cooled (FC) and zero field-cooled (ZFC) protocols with field directed in the interplanar and intraplanar directions. (c) Heat capacity. (d) Resistance measured in the *ab* plane and its derivative with respect to temperature. (e) Real (χ') part of the AC magnetic susceptibility measured with a 10-Oe oscillating field applied in the intraplanar direction.

with field-cooled and zero field-cooled temperature cycles. In addition, a secondary feature appears in the traces at a temperature of $T^* = 36$ K, both in the in-plane and out-of-plane directions. This temperature is also associated with a change in curvature in the resistivity-temperature curve of a separate sample [Fig. 2(c)]. T^* is also resolved in AC magnetic

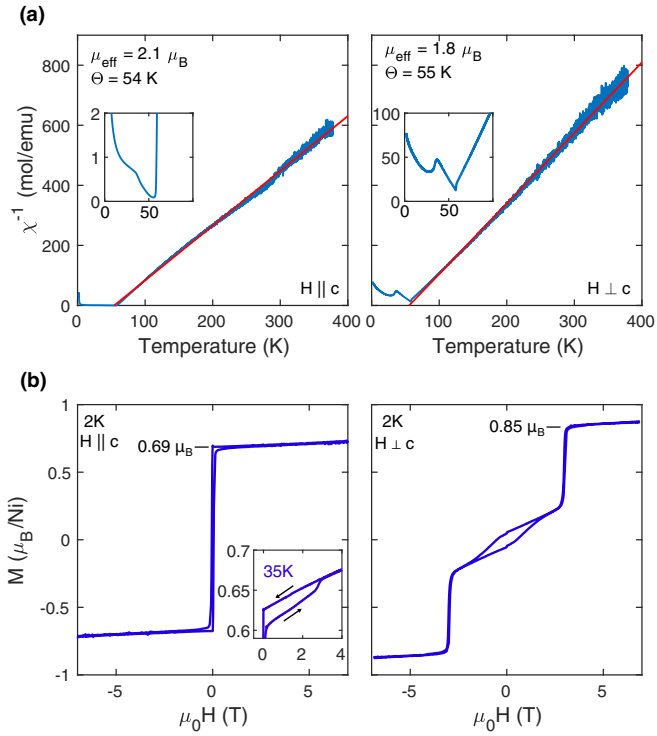

FIG. 3. Magnetization measurements and analysis. (a) Inverse susceptibility versus temperature for the out-of-plane ($H \parallel c$) and in-plane ($H \perp c$) directions. The effective fluctuating moment per nickel atom μ_{eff} extracted from a Curie-Weiss fit (red line) is shown in the panels, along with the Curie temperature Θ. The insets show a zoom in of the inverse susceptibility at low temperature, which shows a double-dip feature. (b) Magnetization versus field hysteresis loops for two crystallographic directions. The out-of-plane loop exhibits a sharp coercive field event, with a saturated magnetic moment of 0.69 bohr magneton per nickel atom. The inset shows that a smaller coercive field event is present at a higher field (see also Fig. S3 [29]). For in-plane magnetic field, there is an apparent metamagnetic transition at a field of about 3 Tesla and the saturated moment is about 0.85 bohr magneton per nickel.

susceptibility measurements on yet another sample [Fig. 2(e)] and in magnetization measurements of polycrystalline powder (Fig. S1) [29]. While the main ferromagnetic-like transition at T_C is clearly resolved in heat capacity measurements, T^* is not, suggesting that T^* might be a phase transition associated with an undetectably small change in entropy, or is not a phase transition at all. The possibility of magnetic impurity phases is addressed in the discussion. Notably, the real part of the AC susceptibility response (χ') is largely independent of the drive frequency between 300 Hz and 10 kHz, and its overall shape is qualitatively similar to that of the DC magnetic susceptibility response shown in Fig. 2(b).

Figure 3 shows the results of magnetic characterization measurements and analysis. Figure 3(a) shows the inverse susceptibility with a fit to the Curie-Weiss law [$\chi = C/(T - \Theta)$], where Θ is the Curie temperature and C is a coefficient proportional to the effective moment ($C = N\frac{\mu_0\mu_{\text{eff}}}{3k_B}$), where μ_{eff} is the effective moment and N is the concentration of moments in the material. For field in both the in-plane and out-of-plane configurations, a similar Curie temperature is found (54–55 K), which agrees well with the observed ordering temperature. With the assumption that the magnetism arises purely from the nickel ions, the fluctuating effective moments are 2.1 μ_B/Ni and 1.8 μ_B/Ni for the out-of-plane and in-plane configurations, respectively, consistent with the magnetic moment associated with a nickel ion in the Ni^{2+} oxidation state. On the other hand, as shown in Fig. 3(b), the saturated moment taken from low-temperature isothermal magnetization field sweeps is found to be 0.69 and 0.85 μ_B per nickel for the out-of-plane and in-plane directions, respectively. Thus, the saturated moment appears to be considerably smaller than the value of the effective Curie-Weiss moment for both crystallographic directions. Such a disparity is a hallmark of itinerant ferromagnetism [12,13]. Note that for fields in the interplanar direction, a secondary coercive field event associated with a tiny magnetic moment (estimated to be about 0.01 μ_B per formula unit at 35 Kelvin) is observed in the hysteresis loops [Fig. 3(b) inset; see also supplemental Fig. S3] [29]. Finally, for the magnetic field directed along the intraplanar direction, a sharp jump in the magnetization is observed at 3 Tesla, an observation, which is most compatible with the presence of a metamagnetic transition. Electrical conductance measurements up to 60 Tesla for a number of field orientations (Fig. S6 [29,32]) confirm that there are no further transitions at higher fields, suggesting that this transition separates the ferromagnetic ground state from the in-plane field-polarized state. The temperature dependence of the coercive field, saturated moment, and metamagnetic transition are explored further in Figs. S3 and S5 [29].

Figure 4 shows angle-resolved photoemission (ARPES) data in comparison to density functional theory (DFT) [33–36] calculations of the band structure and fermiology of the $NiTa_4Se_8$. The ARPES and DFT data seem to agree qualitatively well in both the two-dimensional cut of the Fermi surface through the zone center [Figs. 4(a) and 4(c)], as well as the band structure [Figs. 4(b) and 4(d)]. Broadly speaking, the k_z cut of the Fermi surface through the zone center consists of two large circular electron-like features centered at the K points and more complicated hole-like features at the M point. The electron-like pocket at K is reflected in the band-structure measurements and calculations shown in Figs. 4(d) as a parabolic band crossing the Fermi level, while the complicated set of bands crossing the Fermi level at M produce hole-like pockets. Note also the set of flat electronic bands just above the Fermi level seen in band-structure calculations in Fig. 4(d). The additional spectral weight near $E = 15$ meV in the inset of Fig. 4(b) is likely a signature of these flat bands, indicating their proximity to the Fermi level and therefore potential relevance to the transport and susceptibility functions of $NiTa_4Se_8$.

Consistent with the signatures of flat electron bands in ARPES and DFT calculations, the measured electronic contribution to the heat capacity in $NiTa_4Se_8$ (62 ± 6 mJ/mol K^2) is almost as large as some "heavy fermion" f-electron metals, which typically have electronic heat capacity coefficients between 100 and 1000 mJ/mol K^2. From the heat capacity coefficient, we calculate the density of states at the Fermi level to be 13 ± 1 eV^{-1} u.c.$^{-1}$, which is in quite good agreement with that calculated using DFT (11 eV^{-1}u.c.$^{-1}$). The T^2 coefficient of the resistivity A, typically considered to be

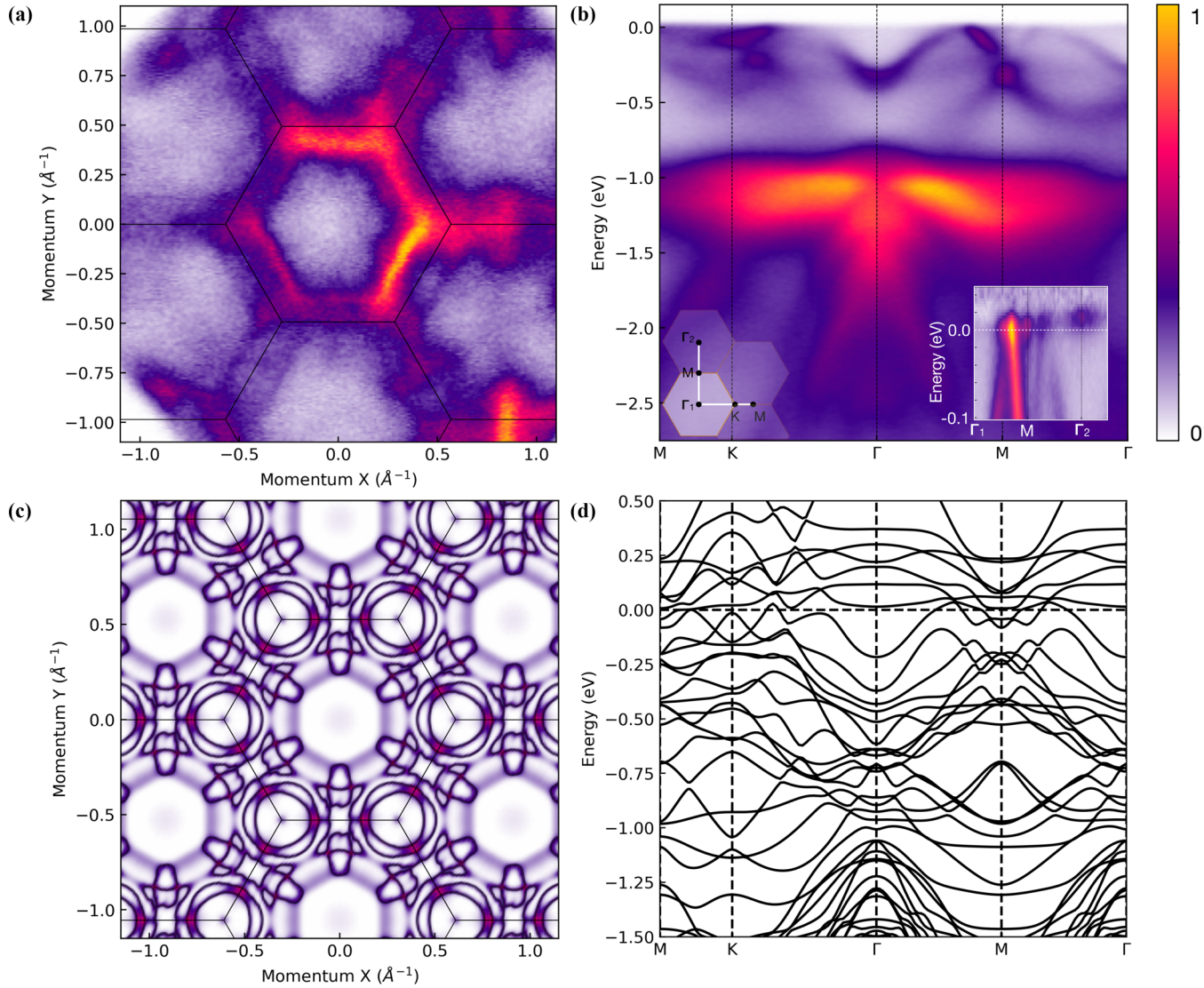

FIG. 4. Electronic structure measurements and calculations. (a) ARPES-measured Fermi surface, acquired at 11 K. Black contours indicate the boundaries of the Brillouin zone of $NiTa_4Se_8$. (b) ARPES-measured band structure along the high-symmetry path indicated in the inset schematic at 10 K. A high-resolution spectrum near the Fermi level is provided in the inset, displayed after division by the resolution-convolved ($dE = 15$ meV) Fermi function. Spectral weight from the thermally occupied flat bands above E_F is most apparent at Γ_2. (c) Two-dimensional Fermi surface projection at $k_z = 0$ for $NiTa_4Se_8$, as computed by DFT. For closer comparison with ARPES, the Fermi surface (black contours) is overlain along with energy-integrated spectral weight spanning $E_F \pm 20$ meV. The hexagonal lattice represents successive neighboring Brillouin zones. (d) Band structure along the same high-symmetry path as surveyed by ARPES in (b), computed by the same DFT solution as in (c).

proportional to the electron-electron scattering rate in Fermi liquids, is 0.032 $\mu\Omega$cm/K^2. These values yield a relatively high Kadowaki-Woods ratio (0.8×10^{-5} $\mu\Omega$mol^{2}K^2/mJ^2), comparable to that observed in f-electron metals [37] and weak itinerant magnets with strong spin fluctuations [23,38]. These results suggest that $NiTa_4Se_8$ hosts strong interelectron interactions, even relative to the high density of electronic states at the Fermi level.

It is often the case that metals with high densities of electronic states and strong interelectron interactions are susceptible to superconducting instabilities [39,40]. Figure 5 explores the emergence of superconductivity in samples where then nickel concentration is reduced during the growth procedure [41]. Crystallographic measurements on these samples are shown in Fig. S10 [29], where we determine that the doped samples are comprised of crystalline $TaSe_2$ layers with disordered layers of nickel between each layer—the nickel is randomly distributed in the reduced concentration lattice. In contrast to the pure material where the ferromagnetic transition is associated with a kink in the resistivity trace, the doped samples exhibit a featureless resistivity trace until a superconducting transition at about 2 Kelvin. Further comparison of the qualitative differences in temperature-dependent resistivity between the two compositions is discussed in Fig. S12 [29,42]. Magnetic susceptibility and heat capacity measurements show relatively pronounced diamagnetism and a prominent heat capacity anomaly, suggesting that the superconductivity is bulk. Note that a small residual heat

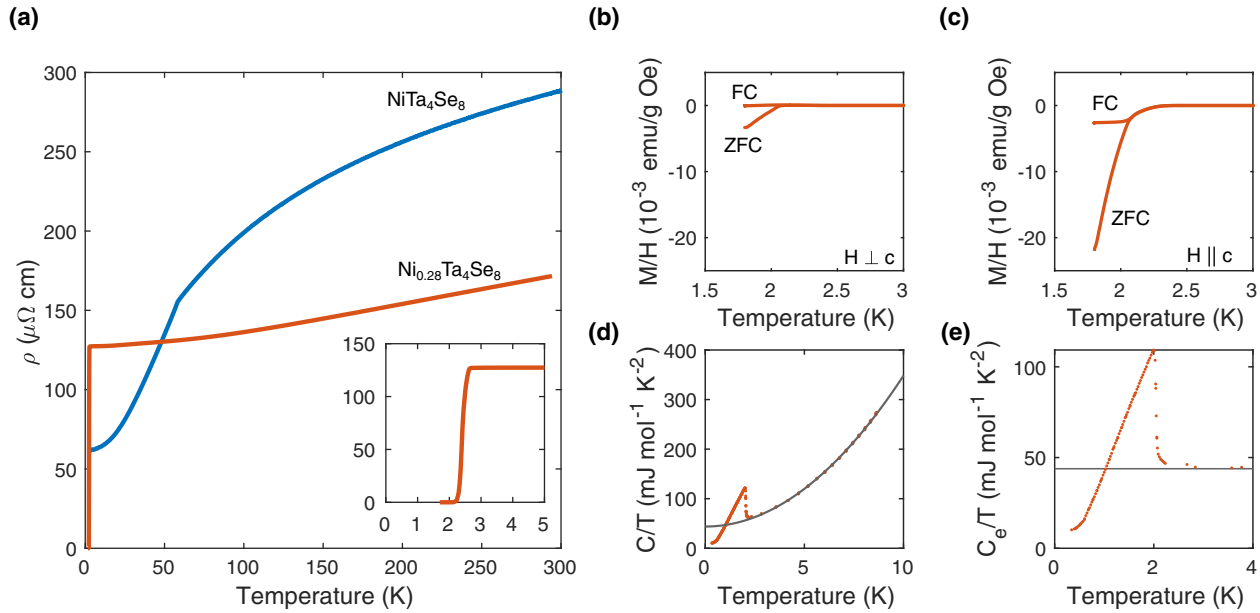

FIG. 5. Superconductivity in doped $Ni_xTa_4Se_8$. (a) Resistivity in pure $NiTa_4Se_8$ and doped $Ni_{0.28}Ta_4Se_8$ with reduced nickel concentration. A clear anomaly in the trace is observed in the pure sample at the ferromagnetic transition, while the doped sample exhibits a featureless curve until a superconducting transition at low temperature. [(b),(c)] Magnetic susceptibility of the doped sample in the field-zooled (FC) and zero field-cooled (ZFC) protocols with a 10-Oe measurement field directed perpendicular and parallel to the crystallographic c-axis. (d) Total heat capacity divided by temperature. The grey line is a fit to the Debye model $C/T = \gamma + \alpha T^2$, where γ is the electron contribution and α is the phonon contribution at low temperature. (e) Temperature-dependent electronic contribution of the heat capacity, determined by subtracting the phonon term from the data in panel (d). A clear superconducting anomaly is observed. The horizontal grey line indicates the normal-state electron contribution to the heat capacity.

capacity appears to persist down to zero temperature even in the superconducting state [Fig. 5(e)]. Measurements of the upper critical field in doped $Ni_xTa_4Se_8$, as well as estimations of the superconducting coherence length in comparison to the mean free path, are presented in Fig. S11 [29]. The intralayer and interlayer coherence lengths are 6.9 ± 0.2 nm and 13.5 ± 1.5 nm, respectively, while the intralayer mean free path is estimated to be roughly 10 nm. From these values, and the strongly anisotropic diamagnetic shielding effect seen in Figs. 5(b) and 5(c), we conclude that the material is a quasi-two-dimensional superconductor in the dirty limit.

Spin-resolved calculations of the electronic structure of $NiTa_4Se_8$ in the magnetic state reveal some interesting correlations. First of all, the Fermi surfaces at the K and M points, respectively, are strongly spin polarized with majority and minority spin electrons, respectively. Given the electronic structure from band-structure calculations and ARPES measurements in Fig. 4, we deduce that the electron and hole-like carriers are separately spin-up and spin-down polarized. There are also qualitative differences in the electronic structures of majority and minority spins in the magnetic state, as summarized in density of states calculations shown in Fig. 6(b), and band-structure calculations in Figs. 6(c) and 6(d). The majority spin band centered at the K point has a high dispersion, while the minority spin bands both of Ta 4d and Ni 3d character are weakly dispersing between the K and M points from above the Fermi level to about 0.25 eV above it—some shallow dispersive pockets at K and M also exist. This manifests in relatively sharp peaks above and below the

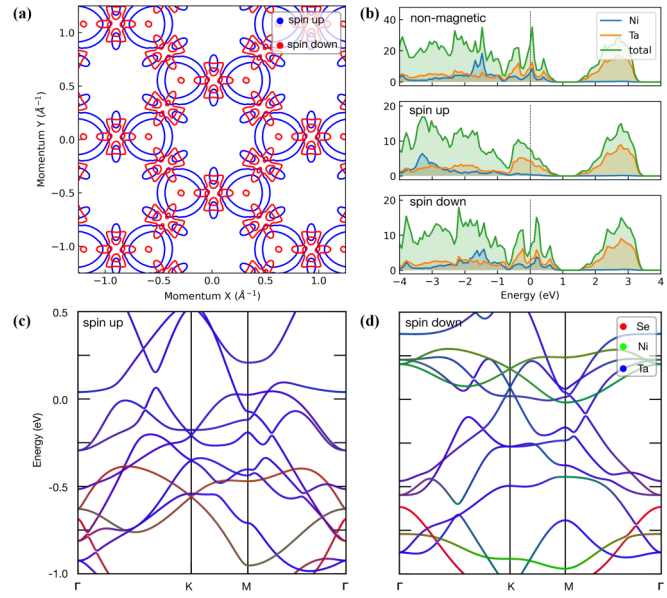

FIG. 6. Spin-resolved electronic structure. (a) Spin-resolved Fermi surface of $NiTa_4Se_8$ in the absence of spin-orbit coupling. Spin-up and spin-down states are indicated in blue and red, respectively. (b) Density of states for nonmagnetic calculation (top), as well as spin-up (middle) and spin-down (bottom) states for spin-polarized calculation. Projection onto Ni and Ta are shown, in addition to the total DOS. (c) Band structure along high-symmetry path for spin-up states; colors encode atomic projection with Se in red, Ni in green and Ta in blue. (d) Same as for (c), but for spin-down bands.

Fermi level in the density of electron states specifically of the minority spin species, while the density of states of the majority spins has a smoother profile overall. Such a difference is rare in ferromagnetic materials, where the density of states of two majority and minority spins are often expected to be qualitatively similar with an overall energy shift given by the magnetic exchange.

IV. DISCUSSION

In $NiTa_4Se_8$, we find evidence of itinerant magnetism in that the saturated magnetic moment, at least on the nickel sites, is nearly three times smaller than the effective Curie-Weiss moment. This effect is even more pronounced in the apparently small magnetic moment generated on the tantalum atoms, presumably in the 4*d* conduction bands with highly itinerant character. Moreover, the material appears to be a strongly correlated metal, as indicated by the peaks in density of states near the Fermi energy [Fig. 6(b)], the high heat capacity coefficient, and the presence of flat bands above the Fermi energy in band structure calculations and ARPES data [Figs. 4(d) and 4(b)].

The interplay between itinerant magnetism and electron correlations may be partially responsible for the superconductivity observed in doped samples (Fig. 5) in analogy to superconductivity near correlated magnetism in graphene heterostructures [3,8] and UTe_2 [5]. Indeed, the specific heat coefficient of $Ni_{0.28}Ta_4Se_8$ [Fig. 5(e)] [29] is only about 30% smaller than that of $NiTa_4Se_8$, indicating that the strong correlations in the parent sample persist in the superconducting composition. However, it is important to note that superconductivity emerges in samples which have a disordered lattice of nickel atoms in contrast to the triangular nickel lattice of the ferromagnetic composition. Nevertheless, exchange interactions between local Ni moments and itinerant TaSe2 electrons are an unavoidable feature of the system, one which is almost certain to either compete with, or contribute to the evolution of superconductivity at low-Ni concentrations. For example, the fully spin-polarized nature of the Fermi surfaces at the *K* points [Fig. 6(a)] in the ferromagnetic compositions of $NiTa_4Se_8$ means that electrons in opposite valleys with the same spin could plausibly pair via ferromagnetic fluctuations in a similar manner to that proposed for graphene heterostructures [8]. Even in electron-phonon based mechanisms, intervalley pairing can support spin-polarized superconductivity—previous theoretical studies suggested that electron-phonon interactions may support triplet pairing in the presence of strong electronic interactions [43] or spin-orbit coupling [44], both of which are present in $Ni_xTa_4Se_8$.

On the other hand, experiments on nonmagnetically doped $TaSe_2$ and disordered $TaSe_2$ suggest that disorder enhances the electron density of states near the Fermi level by suppressing the charge density wave order present in pure 2H-$TaSe_2$ [45–47], thereby increasing the superconducting transition temperature. In our case, it is possible that reduction of the nickel concentration locally enhances the density of states in a similar vein to previous doping studies of $TaSe_2$. However, the clear difference between the situation in Refs. [45–47] and the present scenario is that nickel is a magnetic dopant, which, on general grounds, is expected to suppress superconductivity that is time-reversal symmetric. It is possible that there is a fine-tuning between the competing spin scattering induced in the superconducting condensate by the nickel atom and its local enhancement of the density of states. The nickel layers would then induce triplet correlations in the $TaSe_2$ electrons through a proximity effect in analogy to artifical superconductor/ferromagnet heterostructures [48]. Beyond such proximity effect mechanisms, another possibility is that the conduction electrons of $TaSe_2$ screen the magnetic impurities in doped Ni_xTaSe_2 in analogy to *f*-electron metals—this mechanism would result in the development of subgap states near the magnetic impurities when the sample goes superconducting, which could be detected by local tunneling probes [49].

Aside from the superconductivity and strong correlations, the magnetism itself in $NiTa_4Se_8$ is notable. Specifically, the apparently two magnetic transitions T_C and T^* (Fig. 2), the bipartite structure in the out-of-plane hysteresis loops [Fig. 3(b)], and the metamagnetic transition for in-plane fields all warrant further discussion. Because T^* appears as a rather broad feature [Fig. 2(a)], and lacks a significant heat capacity anomaly, it is important to address the possibility of magnetic impurity phases as a source of this anomaly. The most likely candidates are NiSe [50] and $NiSe_2$ [51] both of which have ferromagnetic ordering temperatures near 20 K. However, the secondary feature (T^*) in susceptibility data on our $NiTa_4Se_8$ crystal occurs closer to 36 K. In addition, our PXRD data do not show evidence of peaks associated with either NiSe or $NiSe_2$, suggesting that any potential impurity phases constitute an undetectably small fraction of the samples. In addition, both resistivity [Fig. 2(b)] and Hall effect (Fig. S2) [29,52] on single crystal samples exhibit crossover features across 36 K, and susceptibility data on powder also exhibits an anomaly at this temperature (Fig. S1) [29]. For these reasons, we believe that T^* is likely to be an intrinsic feature of $NiTa_4Se_8$. Finally, the frequency-independence of T^* in AC susceptibility measurements [Fig. 2(e)] implies that T^* does not correlate to spin-glass physics, which often arises in frustrated magnets [53].

The simplest interpretation, motivated in part by our density functional theory calculations, is that the material has two distinct ferromagnetic moments, and T^* corresponds to the freezing temperature of the relatively small tantalum moments while T_C corresponds to the freezing temperature of the nickel moments. In itinerant magnets, the jump in heat capacity at the ferromagnetic transition is directly proportional to the size of the ordered moment squared [54]—thus, the small value of the ordered tantalum moment may explain the apparent absence of T^* in heat capacity measurements. The bipartite structure of out-of-plane hysteresis loops is also consistent with the magnetic structure put forward in Fig. 1(d)—based on a phenomenological free energy model with two order parameters corresponding to the nickel and tantalum moments, respectively, we are able to reproduce the qualitative structure in the out-of-plane hysteresis loops (Fig. S8) [29]. These simulations assume a single magnetic domain and uniaxial anisotropy, as expected to first order for hexagonal crystals. Note, however, that the bipartite structure in magnetization loops persists above T^* (Fig. S3) [29]. In addition, this free

energy model does not reproduce the inner hysteresis loop for fields directed in-plane [Fig. 3(b)].

A central feature in the data, which is not captured immediately by the magnetic structure in Fig. 1(d), is the presence of a metamagnetic transition for fields directed along the hard axis. We suggest that this feature may originate in the electronic structure of the material. Conventionally in easy axis ferromagnets, one expects a field directed perpendicular to the easy axis to induce a gradual rise in the magnetization until a saturated moment is reached (as exemplified in simulations shown in Fig. S8 [29]). However, there are cases where a metamagnetic transition was observed in ferromagnets with strong anisotropy for fields directed perpendicular to the easy axis, perhaps most notably in compounds like URhGe and UTe_2 where such a transition coincides with reentrant superconductivity [4,55,56]. In other cases, like the itinerant ferromagnets $LuCo_3$, a metamagnetic transition was observed under similar field configurations relative to the easy axis and attributed to a field-induced change in occupancy of d-electron states, which at a critical field causes a redistribution of the majority and minority spin density of states giving a jump in the net magnetization [57]. This essential mechanism for "itinerant electron metamagnetism"—that of field-induced changes to the electronic structures of majority and minority spin species [58]—was considered for several decades to describe metamagnetic transitions in a variety of itinerant ferromagnets [59,60]. The necessary conditions for the presence of itinerant metamagnetism are that the density of states is relatively large and has positive curvature near the Fermi level [58], which causes different free-energy terms to compete with each other at finite field. These conditions are certainly fulfilled in $NiTa_4Se_8$ according to our spin-resolved density-of-states calculations and heat capacity measurements. Indeed, the overall field-temperature phase diagram shown in supplement Fig. S5 [29] is reminiscent of that of itinerant ferromagnetic systems [61], where the transition becomes first order at low temperature.

It remains to be seen how the itinerant metamagnetic transition in $NiTa_4Se_8$ contrasts with that in URhGe or UTe_2, where such a transition is associated with reentrant superconductivity, presumably because of the proliferation of magnetic fluctuations that enhance the pairing susceptibility. Given the apparent proximity of $NiTa_4Se_8$ to superconductivity and the overall similarity in the magnetic phase diagram between $NiTa_4Se_8$ and URhGe, it would be worthwhile to explore the potential emergence of superconductivity at lower temperatures near the metamagnetic transition in $NiTa_4Se_8$. This may prove useful in comparing the physics of heavy fermions to that of the newly discovered unconventional superconductors in layered Van der Waals materials [1,2].

V. CONCLUSION

In this work, we presented the synthesis and characterization of a new magnetically intercalated transition metal dichalcogenide $NiTa_4Se_8$. The system is best described as an itinerant ferromagnet, with spin-polarized electronic states in both the local Ni 3d moments and the more itinerant Ta 4d states. By diluting the Ni concentration by a factor of roughly 4, superconductivity is observed. We suggested a few possible mechanisms for the proliferation of superconductivity in magnetically doped samples near an itinerant ferromagnetic phase. $NiTa_4Se_8$ is likely not unique among the magnetic TMDs, and it may prove fruitful to look for correlated itinerant magnetism and superconductivity in $TaSe_2$ doped with other magnetic intercalants.

ACKNOWLEDGMENTS

This work was supported by the LBNL Quantum Systems Accelerator, funded by the U.S. Department of Energy, Office of Science, National Quantum Information Science Research Centers. A portion of this work was performed at the National High Magnetic Field Laboratory, which is supported by the National Science Foundation Cooperative Agreement No. DMR-1644779 and the State of Florida. We thank Nobumichi Tamura for assistance with microdiffraction measurements. This research used resources of the Advanced Light Source, which is a DOE Office of Science User Facility under Contract No. DE-AC02-05CH11231.

[1] J. Kang, B. A. Bernevig, and O. Vafek, Phys. Rev. Lett. **127**, 266402 (2021).
[2] A. Kumar, N. C. Hu, A. H. MacDonald, and A. C. Potter, Phys. Rev. B **106**, L041116 (2022).
[3] Y. Cao, J. Park, K. Watanabe, T. Taniguchi, and P. Jarillo-Herrero, Nature (London) **595**, 526 (2021).
[4] F. Lévy, I. Sheikin, B. Grenier, and A. Huxley, Science **309**, 1343 (2005).
[5] S. Ran, C. Eckberg, Q.-P. Ding, Y. Furukawa, T. Metz, S. R. Saha, I.-L. Liu, M. Zic, H. Kim, J. Paglione *et al.*, Science **365**, 684 (2019).
[6] H. Zhou, L. Holleis, Y. Saito, L. Cohen, W. Huynh, C. Patterson, F. Yang, T. Taniguchi, K. Watanabe, and A. Young, Science **375**, 774 (2022).
[7] J. Lee, E. Khalaf, S. Liu, X. Liu, Z. Hao, P. Kim, and A. Vishwanath, Nat. Commun. **10**, 5333 (2019).
[8] X. Liu, Z. Hao, E. Khalaf, J. Lee, Y. Ronen, H. Yoo, D. Haei Najafabadi, K. Watanabe, T. Taniguchi, A. Vishwanath *et al.*, Nature (London) **583**, 221 (2020).
[9] K. Law and P. Lee, Proc. Natl. Acad. Sci. **114**, 6996 (2017).
[10] A. Ribak, R. Skiff, M. Mograbi, P. Rout, M. Fischer, J. Ruhman, K. Chashka, Y. Dagan, and A. Kanigel, Sci. Adv. **6**, eaax9480 (2020).
[11] T. Moriya and Y. Takahashi, Annu. Rev. Mater. Sci. **14**, 1 (1984).
[12] Y. Takahashi, *Spin Fluctuation Theory of Itinerant Electron Magnetism*, Vol. 9, (Springer, New York, 2013).
[13] P. Rhodes and E. P. Wohlfarth, Proc. R. Soc. London A **273**, 247 (1963).
[14] T. Moriya and A. Kawabata, J. Phys. Soc. Jpn. **34**, 639 (1973).
[15] T. Moriya, J. Magn. Magn. Mater. **100**, 261 (1991).
[16] D. Fay and J. Appel, Phys. Rev. B **22**, 3173 (1980).

[17] S. Hoshino and Y. Kuramoto, Phys. Rev. Lett. **111**, 026401 (2013).

[18] B. Shen, Y. Zhang, Y. Komijani, M. Nicklas, R. Borth, A. Wang, Y. Chen, Z. Nie, R. Li, X. Lu *et al.*, Nature (London) **579**, 51 (2020).

[19] L. Fenner, A. Dee, and A. Wills, J. Phys.: Condens. Matter **21**, 452202 (2009).

[20] C. Gong, C. Li, Z. Li, H. Ji, A. Stern, Y. Xia, T. Cao, W. Bao, C. Wang, Y. Wang *et al.*, Nature (London) **546**, 265 (2017).

[21] B. Huang, G. Clark, E. Navarro-Moratalla, D. Klein, R. Cheng, K. Seyler, D. Zhong, E. Schmidgall, M. McGuire, D. Cobden *et al.*, Nature (London) **546**, 270 (2017).

[22] S. Doniach and S. Engelsberg, Phys. Rev. Lett. **17**, 750 (1966).

[23] W. F. Brinkman and S. Engelsberg, Phys. Rev. **169**, 417 (1968).

[24] A. Tonomura, X. Yu, K. Yanagisawa, T. Matsuda, Y. Onose, N. Kanazawa, H. Park, and Y. Tokura, Nano Lett. **12**, 1673 (2012).

[25] M. Brando, D. Belitz, F. M. Grosche, and T. R. Kirkpatrick, Rev. Mod. Phys. **88**, 025006 (2016).

[26] R. Ritz, M. Halder, M. Wagner, C. Franz, A. Bauer, and C. Pfleiderer, Nature (London) **497**, 231 (2013).

[27] A. Pogrebna, T. Mertelj, N. Vujičić, G. Cao, Z. A. Xu, and D. Mihailovic, Sci. Rep. **5**, 7754 (2015).

[28] N. F. Berk and J. R. Schrieffer, Phys. Rev. Lett. **17**, 433 (1966).

[29] See Supplemental Material at http://link.aps.org/supplemental/10.1103/PhysRevB.106.224429 for additional data and description of methods.

[30] E. Morosan, H. W. Zandbergen, L. Li, M. Lee, J. G. Checkelsky, M. Heinrich, T. Siegrist, N. P. Ong, and R. J. Cava, Phys. Rev. B **75**, 104401 (2007).

[31] B. Van Laar, H. M. Rietveld, and D. J. W. Ijdo, J. Solid State Chem. **3**, 154 (1971).

[32] M. Altarawneh, C. Mielke, and J. Brooks, Rev. Sci. Instrum. **80**, 066104 (2009).

[33] G. Kresse and J. Hafner, Phys. Rev. B **48**, 13115 (1993).

[34] G. Kresse and J. Furthmüller, Phys. Rev. B **54**, 11169 (1996).

[35] J. Sun, A. Ruzsinszky, and J. P. Perdew, Phys. Rev. Lett. **115**, 036402 (2015).

[36] A. Ganose, A. Jackson, and D. Scanlon, J. Open Source Softw. **3**, 717 (2018).

[37] K. Kadowaki and S. Woods, Solid State Commun. **58**, 507 (1986).

[38] A. K. Mishra, M. Krishnan, D. Singh, S. S. Samatham, M. Gangrade, R. Venkatesh, and V. Ganesan, J. Magn. Magn. Mater. **448**, 130 (2018).

[39] P. A. Lee, N. Nagaosa, and X.-G. Wen, Rev. Mod. Phys. **78**, 17 (2006).

[40] C. Pfleiderer, Rev. Mod. Phys. **81**, 1551 (2009).

[41] L. Li, Y. Sun, X. Zhu, B. Wang, X. Zhu, Z. Yang, and W. Song, Solid State Commun. **150**, 2248 (2010).

[42] D. Goodings, Phys. Rev. **132**, 542 (1963).

[43] H. Shimahara, arXiv:cond-mat/0403628.

[44] V. I. Fal'ko and B. N. Narozhny, Phys. Rev. B **74**, 012501 (2006).

[45] A. Chikina, A. Fedorov, D. Bhoi, V. Voroshnin, E. Haubold, Y. Kushnirenko, K. Kim, and S. Borisenko, npj Quantum Mater. **5**, 22 (2020).

[46] L. Li, X. Deng, Z. Wang, Y. Liu, M. Abeykoon, E. Dooryhee, A. Tomic, Y. Huang, J. Warren, E. Bozin *et al.*, npj Quantum Mater. **2**, 11 (2017).

[47] S.-H. Baek, Y. Sur, K. Kim, M. Vojta, and B. Büchner, New J. Phys. **24**, 043008 (2022).

[48] A. I. Buzdin, Rev. Mod. Phys. **77**, 935 (2005).

[49] E. Liebhaber, S. Acero Gonzalez, R. Baba, G. Reecht, B. Heinrich, S. Rohlf, K. Rossnagel, F. von Oppen, and K. Franke, Nano Lett. **20**, 339 (2019).

[50] N. Umeyama, M. Tokumoto, S. Yagi, M. Tomura, K. Tokiwa, T. Fujii, R. Toda, N. Miyakawa, and S.-I. Ikeda, Jpn. J. Appl. Phys. **51**, 053001 (2012).

[51] S. Yano, D. Louca, J. Yang, U. Chatterjee, D. E. Bugaris, D. Y. Chung, L. Peng, M. Grayson, and M. G. Kanatzidis, Phys. Rev. B **93**, 024409 (2016).

[52] N. Nagaosa, J. Sinova, S. Onoda, A. H. MacDonald, and N. P. Ong, Rev. Mod. Phys. **82**, 1539 (2010).

[53] E. Lachman, R. Murphy, N. Maksimovic, R. Kealhofer, S. Haley, R. McDonald, J. Long, and J. Analytis, Nat. Commun. **11**, 560 (2020).

[54] J. Clinton and R. Viswanathan, J. Magn. Magn. Mater. **1**, 73 (1975).

[55] V. P. Mineev, Phys. Rev. B **91**, 014506 (2015).

[56] G. Knebel, W. Knafo, A. Pourret, Q. Niu, M. Vališka, D. Braithwaite, G. Lapertot, M. Nardone, A. Zitouni, S. Mishra *et al.*, J. Phys. Soc. Jpn. **88**, 063707 (2019).

[57] D. S. Neznakhin, D. I. Radzivonchik, D. I. Gorbunov, A. V. Andreev, J. Šebek, A. V. Lukoyanov, and M. I. Bartashevich, Phys. Rev. B **101**, 224432 (2020).

[58] E. Wohlfarth and P. Rhodes, Philos. Mag. **7**, 1817 (1962).

[59] R. Levitin and A. Markosyan, J. Magn. Magn. Mater. **177-181**, 563 (1998).

[60] M. Shimizu, J. Physique **43**, 155 (1982).

[61] D. Belitz, T. R. Kirkpatrick, and J. Rollbühler, Phys. Rev. Lett. **94**, 247205 (2005).